Journal of Materials Chemistry A

Nature of Terrace Edge States (TES) in Lower-Dimensional Halide Perovskite

Journal:	*Journal of Materials Chemistry A*
Manuscript ID	TA-COM-01-2020-000523.R1
Article Type:	Communication
Date Submitted by the Author:	05-Mar-2020
Complete List of Authors:	Wang, Kai; Virginia Tech, Center for Energy Harvesting Materials and System; Virginia Tech Wu, Tao; University of South Carolina, Wu, Congcong ; Pennsylvania State University, Materials Science and Engineering Sriramdas, Rammohan ; Pennsylvania State University, Materials Science and Engineering Huang, Xu; University of Electronic Science and Technology of China, Research Branch of Functional Materials Wang, Ke; The Pennsylvania State University, Materials Research Institute Jiang, Yuanyuan; Pennsylvania State University, Materials Science and Engineering Liu, Hairui; Pennsylvania State University, Yan, Yongke; Penn State University Park Yang, Dong; Pennsylvania State University, Materials Science and Engineering Ye, Tao; Pennsylvania State University, Materials Science and Engineering LIU, CHANG; Ningbo Institute of Materials Technology and Engineering CAS Hu, Xiaowen; South China Normal University Guangzhou Higher Education Mega Center, South China Academy of Advanced Optoelectronics Jiang, Xiaofang; South China Normal University, Priya, Shashank; Pennsylvania State University

Nature of Terrace Edge States (TES) in Lower-Dimensional Halide Perovskite

Kai Wang,*[#1] Tao Wu,[#2] Congcong Wu,[#3] Rammohan Sriramdas,[1] Xu Huang,[4] Ke Wang,[1] Yuanyuan Jiang,[1] Hairui Liu,[1] Yongke Yan,[1] Dong Yang,[1] Tao Ye,[1] Chang Liu,[5] Xiaowen Hu,[6] Xiaofang Jiang,[6] Shashank Priya*[1]

[1] Materials Research Institute, The Pennsylvania State University, University Park, PA 16802, United States
[2] Department of Mechanical Engineering, University of South Carolina, Columbia, SC 29208, United States
[3] Hubei Collaborative Innovation Center for Advanced Organic Chemical Materials, Key Laboratory for the Green Preparation and Application of Functional Materials, Hubei Key Laboratory of Polymer Materials, School of Materials Science and Engineering, Hubei University, Wuhan 430062, China
[4] School of Materials Science and Engineering, Southwest University of Science and Technology, Mianyang, Sichuan 621010, PR China
[5] Ningbo Institute of Materials Technology and Engineering (NIMTE), Chinese Academy of Science (CAS), Ningbo, Zhejiang 315201, PR China
[6] South China Academy of Advanced Optoelectronics, South China Normal University, Guangzhou 510006, PR China

Abstract

Lower-dimensional quasi-two-dimension (quasi-2D) halide perovskites have emerged as promising building blocks for multiple optoelectronic applications due to their superior photophysical properties. Recently, there is a research focus on the terrace edge states (TES) in quasi-2D perovskites, which is thought to provide hypothetical highways to transport the excited states and thus give a new insight to boost relevant device performance. Nevertheless, there is neither direct evidence on the electronic facet nor the in-depth understanding of these newly observed nontrivial TES. Here, we are the first to directly visualize the highly charge concentrated TES by means of a charge gradient microscopy (CGM) technique and elucidate the nature of TES through a combination of microscopic characterizations, including high-resolution transmission electron microscopy, Kelvin probe force microscopy and confocal fluorescence microscopy coupled with a first-principle density function theory (DFT) calculation. It is shown that TES of the quasi-2D perovskites are highly conductive (in distinct contrast to the insulating flat terrace region) and display higher Fermi-level and smaller forbidden bandwidth, which is attributed to the unique electron orbitals of Pb atom at the terrace edges. This distinctive conductive TES is of great importance in distinguishing them from their bulk physical properties and inspiring novel nanoscale electronic applications such as tip-based data storage and triboelectric nanogenerators.

[#]These authors equally contribute to this work.
*Corresponding author: Email: kaiwang@psu.edu (K.W.), sup103@psu.edu (S.P.)

1. Introduction

Quasi-two-dimensional (Quasi-2D) perovskites are promising semiconducting materials offering great opportunities to develop host of platforms for the next-generation of optoelectronics including solar cells, light-emitting diode (LED), detectors, laser diodes, *etc*.[1–4] Superior physical properties of quasi-2D perovskite can be related to their high light extinction coefficient, excellent electronic properties, high defect tolerance and lack of non-radiative deep level traps.[5,6] Various implementations taking advantages of these bulk physical properties of quasi-2D perovskite have been developed. Recently, quasi-2D perovskite based optoelectronic implementations including solar cells, photodetectors, transistors, and memory devices have been well reviewed elsewhere.[7] However, the fundamental understanding of several relevant material characteristics at molecular scale remains unclear. One such less understood issue is the nature and functionality of the terrace edge states (TES) in quasi-2D perovskites.[8–10]

The TES in typical low-dimensional inorganics can make a big difference to the bulk physical properties due to the localized structural asymmetry. For example, in 2D HgTe quantum wells (QWs), the nontrivial edge states enable the dissipationless one-dimensional (1D) conduction along the TES.[11] And in several multiple-quantum-well (MQW) systems, the existence of Majorana fermions enables the superconductivity at the quantum spin Hall edges.[12] The electronic properties in graphene also display a strong dependence on the atomic configurations at the terrace edges.[13] In terms of the quasi-2D perovskites, recent studies have suggested the presence of the red-shifted "emissive" TES, where lower energy states could accumulate at the 2D crystal terrace edges and facilitate charge dissociation there.[14] Wang *et al.* observed the brighter luminescent TES of $CsPb_2Br_5$ microplatelets.[15] And our prior study also revealed a high carrier density of $\sim 10^{21}$ cm^{-3} at the TES in BA_2PbI_4 2D MQW structures. These studies indicate that the TES can be host for the excited charge carriers and responsible for the transport of excited states. While arguments on the chemically induced new phase instead of a localized electronic state have been raised to the TES.[16] So far, the nature of the formation of TES in quasi-2D perovskite still remains debate. In parallel, prior studies relying on non-contact characterization techniques did not give a direct evidence of the conductive TES in general quasi-2D perovskite.[14,15]

Here in this study, we first visualize the distinct conductive TES among the insulating terrace regions and then manifest the nature of these states in quasi-2D perovskite by means of a combination of multiple microscopic characterizations coupled with a first-principle density

function theory (DFT) calculation. We confirm by employing the charge gradient microscopy (CGM)[17,18] that the highly conductive TES exists in all the quasi-2D perovskites (including 2D and 3D perovskite), regardless of the quantum well thickness. In addition, the TES is observed to have higher Fermi-level and lower optical bandgap. We further depict the electronic reconstruction picture calculated using DFT and manifest that the nontrivial electronic properties of TES can be ascribed to the unique electron orbitals of Pb atom at the structural asymmetric terrace edge.

2. Results and discussion

In our prior studies, conducting atomic force microscopy (C-AFM) has been utilized to interrogate the "insulating/conducting/insulating" feature across the terrace edge of BA_2PbI_4 2D MQWs,[19] but fail to distinguish the TES in more conductive quasi-2D and 3D perovskites. Typical C-AFM or current-sensing AFM (CS-AFM) requires external bias to drive the charge flow for the current detection, which would also cause the tunneling current within the flat terrace region, blunting the edge current signal. While in the case of quasi-2D perovskite with larger quantum well (QW) thickness or in the case of 3D perovskite, as the bulk terraces become more conductive,[2] stronger current detection in the flat terrace region will significantly interfere with the current detection at the crystal edges, causing the edge current to be less distinguishable. To decouple the terrace current influence, here we employed the CGM to image the edge current in these more conductive quasi-2D and 3D perovskites. **Figure 1A** shows the schematics of a MQW structure of $BA_2MA_3Pb_4I_{13}$ (n = 4), with BA being butylammonium, MA being methylammonium, Pb being lead, I being iodide and n = 4 featuring the layers number of [PbI_6] octahedra stacking. **Figure 1B** shows the layout of CGM technique, which relies on the dynamic consumption and refilling of the charges by the movement of conductive microprobe on the sample surface.[17] More importantly, CGM requires both the tip and samples being grounded during the measurement to ensure no charge injection at the terrace regions and hence no bulk current flow throughout the sample. We employed the single-crystalline 2D, quasi-2D and 3D perovskite flakes and oriented their out-of-plane directions to be parallel to the vertical direction (z-direction) of the CGM tip. Thus, the CGM scanning direction is parallel with the QW plane of the samples. Schematically, a MQW-structured quasi-2D halide perovskite sample is depicted with flat terrace region and sharp terrace edge (**Figure 1B**). We employed the single-crystalline flake sample to ensure the in-plane scanning and out-of-plane CGM detection throughout the whole sample. The single-crystalline perovskite flakes

were synthesized through a floating method reported elsewhere,[2,20] and the phase purity was verified by X-ray diffraction (**Fig. S1** in **Supporting Information 1** (**SI1**)). **Figure 1C** displays the laminar MQW structure by scanning electron microscope (SEM) measurement, and the inset shows a photograph of a centimeter sized single-crystalline flake of $BA_2MA_3Pb_4I_{13}$. The sample orientation on a grounded substrate was verified by X-ray diffraction (XRD) measurement (see **SI 1** for more details). The scanning was conducted in dark condition to eliminate the bulk photovoltaic influence. Further details on the CGM measurement are given in **Experimental Section**.

To exclude the impurity concerns on the TES, we employ the high-resolution transmission electron microscopy (HRTEM) to investigate these crystal terrace edges. It appears that the crystal edge exhibits a clean crystalline feature, without any additional attachment of unbonded ions or impurities (**Figs. S3a&b** in **SI 1**). **Figure 1D** displays the HRTEM image of a $BA_2MA_3Pb_4I_{13}$ (n = 4) perovskite crystal with a clear terrace edge contour. To identify the atomic arrangement at the terrace edge, we analyze the local HRTEM images along the terrace edge contour (denoted by 19 white squares), and compare them to the flat terrace regions (i.e., both top- and bottom-layer regions). The fast Fourier transform (FFT) implies the terrace edge shares the same atomic arrangement to the flat terrace regions (**Figure 1E**), with strong diffraction spots at (201) and (022), corresponding to the identical spacing d{201} of 4.0 Å and d{022} of 4.4 Å. To further probe the chemical composition across the terrace edge, we characterize the sample using the confocal Raman technique. **Figure 1F** shows the optical-microscopy images of a quasi-2D crystal with clear terrace edges. A squared region is utilized for the confocal Raman mapping (**Figure 1G**). **Figure 1H** compares the Raman spectra between terrace edge regions, flat top-layer and bottom-layer regions. It is found the terrace edge region shares the identical Raman spectrum to those from flat terrace regions. Strong signals at 94 cm^{-1} for Pb-I bending and characteristic response at 1475 cm^{-1} for CH_2 bending, and 3000 cm^{-1} for C-H stretching have been detected. Overall, both HRTEM and confocal Raman measurements suggested there is no exotic impurities or foreign chemicals accumulated at the crystal terrace edges.

Figure 2 shows the CGM topography and current images of different perovskite samples. By mapping different perovskite samples of $BA_2MA_{n-1}Pb_nI_{3n+1}$ with n = 1, 2, 4 and ∞, we find that the flat terrace region remains insulating with zero current detection, while at the terrace edges all samples exhibit distinct current signal. Topographically, in the flat terrace regions, the flakes

exhibit atomically smooth surface with different altitudes. At the edge of each terrace layer, there are sharp layer edges forming the terrace edge regions. An average line profile was extracted along the dashed arrow direction from the topography and current images of each sample to quantify the current change across the edge. As shown in **Figure 2C, F, I, L**, the current spikes occur exactly at the position where the terrace edges are located. It should be noted that such an edge current exists in the whole series of halide perovskite materials from 2D to quasi-2D to 3D, regardless of the QW thickness or the stacking index *n*. Interestingly, we found as the scan direction changes, the current spikes flip as well. For example, in **Figure 2C, F** (when n =1 and 2, respectively, in trace scan direction), scanning from low-height region to high-height region exhibits a negative current; while in **Figure 2I, L** (when $n = 4$ and ∞, respectively, in trace scan direction), scanning from high-height region to low-height region exhibits a positive current. This current direction flip will be discussed later. Meanwhile in **Figure 2C, F**, a small negative current of *ca.* -5 pA with a single spike was observed in $n = 1$ sample, while a higher negative current with two spikes was observed in $n = 2$ sample. Similar current spike splitting is observed in $n = 4$ sample. The two spikes observed in **Figure 2F, I** are due to the presence of two terrace edge stages. Overall, at the terrace edge, clear nonzero current has been observed. Prior research using non-contact photoluminescence techniques suggested that there was a big difference in the light emission property at the edge states between small QW samples ($n \leq 2$, *e.g.,* BA_2PbI_4 ($n = 1$) and $BA_2MAPb_2I_7$ ($n = 2$)) and large QW samples ($n > 2$, *e.g.,* $BA_2MA_3Pb_4I_{17}$).[14] While using contact measurements here, we consistently observed the current detection at the terrace edges regardless of the QW thicknesses. Particularly, even in the limit case of 2D MQW of BA_2PbI_4 ($n = 1$), edge current is clearly observed. More interestingly, for the 3D perovskite of $MAPbI_3$ ($n = \infty$), there exists sharp edge current in the neighbor of the zero-current flat terrace region, suggesting that the conductive TES exist extensively in halide perovskites regardless of the structural dimensionality.

To quantify these TES, we then tune the scan frequency, terrace edge height, loading force and scan direction to track the resultant current signal from the CGM technique. We took the $BA_2MA_3Pb_4I_{13}$ ($n = 4$) sample as an example to quantify these effects. **Figure 3A** shows the CGM current images of the same area scanned at different frequencies from 0.2 Hz to 3.5 Hz. The corresponding current profiles along the in-plane *x*-direction are compared in **Figure 3B**. As the scan frequency gradually increases, the current in flat terrace regions remains constantly zero, whereas the terrace edges exhibit increased currents along with the frequency. The peak current at

the same position of x = 28.3 μm (dash line in **Figure 3B**) is plotted as a function of the scan frequency (**Figure 3C**). A linear relationship is observed between the TES current and scan frequency. This is consistent with the typical CGM results in ferroelectric samples where the domains wall current linearly scales with the tip velocity.[21] In addition to the peak current, we calculated the total charge collected across the edge by using **Eq. (1)**:

$$Q = \frac{\int I(x)dx}{2Lf} \qquad (1)$$

with Q being the total collected charges across the edge, $I(x)$ is the current profile along in-plane x-direction (**Figure 3B**), L is the scan size and f is the frequency (detailed derivation is shown in **SI 2**). The current integration with respect to x (*i.e.,* $\int I(x)dx$ in **Fig. S4b**) is proportional to the scan frequency (**Fig. S4c**), indicating that the total collected charges across the edge is constant regardless of the scan frequencies (**Fig. S4d**). The average total collected charges are calculated to be 175 ± 32 fC (detailed in **SI 2**).

Figure 3d shows the 3D topography and current landscapes where different edge heights are presented. A line profile is extracted in the x-direction to compare with the current at edges of different heights, along with the corresponding height profiles (**Figure 3E**). The current shows a higher magnitude at the terrace edge that has a larger edge height. For example, at a smallest edge height of 3.2 nm (edge position '*1*' in **Figure 3E**, corresponding to one-layer thick QW of $BA_2MA_3Pb_4I_{13}$ (n = 4), as schematically shown in **Fig. S2k**), a smallest edge current of -3.5 pA is observed. At higher edge height of 9.7 nm (position '*2*'), there is a higher edge current of -12.6 pA. Even higher current of -23.5 pA is found at a larger height of 16.0 nm (position '*3*'). To correlate the edge height with the edge current, we took the first derivative of the height profile (z-profile) with regard to x, *i.e., dz(x)/dx*, and compared it with the current profile in **Figure 3E** (bottom panel). Mathematically, the area under the peak of *dz(x)/dx* denotes the edge height at that position. The area under the peak of $I(x)$ is proportional to the total collected charges across that edge position (**Eq. (1)**). Here we found that both curves of *dz(x)/dx* and $I(x)$ fit well with each other and the area below each peak at different positions shows an excellent coincidence, which indicates a linear relationship between the total collected charges and edge height. **Figure 3F** reveals the linear dependence of the peak current on the edge heights. At different edge heights, across each edge step, the collected net charges are proportional to the edge height difference, Δz (**Fig. S5b**). In the contact mode of CGM with a constant loading force on the probe, the contact area between the probe and the sample surface remains identical (discussed later). Hence, the linear relationship

between charges and the edge height suggests a constant carrier density at the terrace edges. These charge carriers residing at the terrace edges are consistent with previous optical characterizations showing that excited states are at the TES in quasi-2D perovskite such as $BA_2MA_3Pb_4I_{13}$,[14] and $CsPb_2Br_5$.[15] We noticed in this analysis that the number of charge carriers can be quantified by the height difference of the terrace edge step, where a linear charge density of ca. 7.5×10^{-3} pC nm^{-1} is calculated. A larger edge height differences will contribute more conductive states and hence a stronger current signal will be detected. It should be noted that the height difference is correlated with the layer numbers. We then summarized the peak current from different $BA_2MA_{n-1}Pb_nI_{3n+1}$ (n = 1, 2, 4 and ∞) samples (detailed in **Table S1** from **SI 4**). The as measured peak current from different samples are normalized to the unit scan frequency and unit height difference, as they are linearly dependent. The normalized peak current displays a linear dependence on the $l_{QW}/(l_{QW}+l_{QB})$ (**Fig. S7c**), where the l_{QW} is the quantum well thickness and l_{QB} is the quantum barrier thickness, respectively. In principle, the free electrons in semiconductors are mainly at the conduction band minimal in the momentum space. And the electron band edge curvature of halide perovskite is mainly contributed by the *s* and *p* electron orbital from Pb and *p* orbital of I.[22] Our experimental observation shows that the current is more corresponding to the l_{QW} from the [PbI_6] octahedra. This is in accordance to above semiconducting physics that in contrast to the organic spacer, it is the [PbI_6] octahedra that leads to the terrace edge current.

The current at the terrace edge corresponds to the charge transport between the CGM probe and the sample surface. It is well known that for nanoscale Schottky contact, the particular electrode geometry of the nanotip-plane contact (*e.g.,* C-AFM) can induce a significantly intensified local electrical field percolating from the contact area into the inner sample.[23] Excited charges from the sample within the non-uniform electric field can drift or transport towards the tip *via* multiple mechanisms including thermionic emission and quantum tunneling.[24] Hence the edge current intensity can be adjusted through the modulation of the contact area. Using the Hertz model, we employed different loading forces (L) to manipulate the contact area (A), according to the expression[25]

$$A = \pi\left[\frac{r_t L}{\left(\frac{1-{\nu_s}^2}{E_s}+\frac{1-{\nu_t}^2}{E_t}\right)}\right]^{2/3} \qquad (2)$$

where r_t is the tip radius, ν_s and ν_t are Poisson ratios and E_s and E_t are the Young's moduli of the sample and tip, respectively. The "effective area" (A_{eff}) responsible for excited carriers to drift from the sample to the top electrode (CGM tip) can then be estimated from the contact area (A) according to the finite element method or numerical simulation (detailed in **SI 5**).[26] As shown in **Figure 3G**, increasing the loads leads to a higher edge current. We further extracted current profiles along the dash lines in the CGM current image and compared them in **Figure 3H**. The loading force on the CGM tip did not influence the flat terrace region, since there is no charge injection when the tip is scanning the terrace region. Increasing the loading force only enlarges the effective contact area, but never induce any net current flow in the terrace region. Instead, at the terrace edge regions (**Figure 3I**), as the loading force increases from 1.6 nN to 6.0 nN, the edge current displays a negative peak increase from -8.8 pA to -22.1 pA. Further increasing the loading force to 15.0 nN, larger current of -39.2 pA was observed. To better understand the current flow at the tip-sample contact, we normalize the current by dividing the edge current over the effective area (**SI 5**), as the enhanced current could be related to the tip-sample contact area that increases with the loading force. As expected, a nearly invariant current density was observed regardless of the loading force (**Fig. S8d**). Hence, the increase of current upon higher loading force can be explained by the increase in the contact area. The loading force did not show significant influence on the current density.

Typical CGM measurement on ferroelectric material may exhibit a scan direction dependence of the current polarity.[17] Here in the 2D, quasi-2D and 3D perovskite samples, we found that there are either positive or negative current direction depending on the combination of the scan direction and sample topography (**Figure 2**). In the contact mode, the CGM tip moves horizontally on the sample surface, and in *z*-direction (out-of-plane direction perpendicular to the sample surface), the movement of the tip can be either ascending or descending the terrace edge depending on the topographical feature of the sample surface. To understand current polarity dependence on the relative movement of the tip on the sample surface, we utilize a stripe sample with both raised and depressed topographies and track both the trace (scanning from left to right) and retrace (scanning from right to left) scan. As shown in **Figure 4B, C**, at the same edge position, inverted current directions were observed under reversed scan directions. To exemplify, at the first raising edge step on the left (*i.e.,* position *'1'* in **Figure 4A**), in the trace scan, the edge exhibits a negative current; while in the retrace scan, a positive current was observed instead, which also

occurs at position *'3'*. Interestingly, at position *'2'*, a totally opposite observation is made as demonstrated in the corresponding line profile in **Figure 4D-F**. At the same edge position, the scan direction only changes the sign of the current but keeps the current value invariant. For instance, at position *'1'*, trace scan gave a current of -12.6 pA while the retrace scan gave an almost identical value of 12.8 pA. Similar observations can be found in various samples (**Fig. S9** in **SI 6**). This is reasonable as edge height is the same at the same edge position, and the scan rate or the loading force are constant during the trace-retrace scan. Hence the magnitude of the edge current remains the same but the only difference is the current polarity. Furthermore, focusing on the relative movement of tip on sample, we found that every time the tip moves uphill the sample edge, the current shows a negative profile, indicating the electrons are extracted from sample to tip (or can be regarded as hole injection from tip to sample). In contrast, whenever the tip moves downhill the sample edge, the current exhibits a positive profile, suggesting that the electrons are injected from tip to the sample. The mechanism responsible for the relative movement induced current polarity reversion is related to the competing relationship between electron consumption and refilling at the terrace edges. **Figure 4G** shows the schematic of the CGM tip moving uphill the terrace edge. It has been reported that the conducting nanoscale tip in CGM measurement could scrap the domain wall charges on the surface of ferroelectric materilas.[18,21] As detailed in **Figure 4G (ii)**, the scraping of terrace edge electrons by the upward-moving tip leads to the accumulation of electrons at the tip front. These excessive electrons lower the electrical potential at the probe cusp (or can be seen as "hole injection" to the tip to balance the accumulated negative charges there, (**SI 6**)). On the other hand, in the case of tip descending the terrace edge, an electron refilling mechanism takes place. As shown in **Figure 4H (ii)**, during the tip moving downhill the terrace edge, the edge charges are being repelled by the tip front due to the mechanical impact and possibly the repulsive force from neighboring charges.[17] In this condition, the edge electrons are being supplied by the electron injection from the tip and being deposited on the terrace edge (**Figure 4H (iii)**). As such, a current flowing from the sample to the tip is formed, representing a positive current detection. Depending on different tip-sample dynamic interaction, the charge flow is either caused by replenishment (by electron injection) or consumption (by hole injection from the tip). It is noteworthy that the only difference is the switched current direction while the current magnitude remains constant, suggesting that in both situations the density of TES remains constant but

alternate the flow direction. We have shown that this density is determined by the edge height difference of the material itself.

To further understand the conductive TES in quasi-2D perovskite materials and distinguish it from that of typical ferroelectric materials such as the periodically poled lithium niobate (PPLN)[17], we investigated the ferroelectric performance of $BA_2MA_3Pb_4I_{13}$ (n = 4) materials. Both PFM and polarization electric field loop suggest the $BA_2MA_3Pb_4I_{13}$ (n = 4) did not display obvious ferroelectric behavior (detailed in **SI 7**). We then employed the Kelvin probe force microscopy (KPFM) and confocal fluorescence microscopy (CFM) to identify these TES. **Figure 5A** displays the topography and contact potential difference (CPD, between tip and sample) images of a $BA_2MA_3Pb_4I_{13}$ (n = 4) sample. A terrace edge is clearly shown in the topographical image. Correspondingly, in the CPD image, higher CPD response is observed in the same terrace edge region (denoted by the blue parallelogram), compared to that in the flat terrace region. We compared the average CPD profile along the terrace edge geometry with that from the bottom- and top-layer regions (**Figure 5B**). The terrace edge exhibits a higher average CPD of 398 meV than the 337 meV from either flat bottom- or top-layer region. As a result, the terrace edge exhibits a higher Fermi level of -3.66 eV than that of -3.72 eV of the flat bottom- or top-layer region (the tip was calibrated by the highly oriented pyrolytic graphite (HOPG), detailed in **SI 8**). The higher Fermi level is consistent to the higher electron concentration at the terrace edge states detected by CGM. We also mapped the photoluminescence (PL) across the terrace edge region. **Figure 5C** shows the optical-microscopic image of a $BA_2MA_3Pb_4I_{13}$ (n = 4) sample. A monochromic laser with a wavelength of 633 nm was used as the excitation light and **Figure 5D & E** display the CFM mapping probed at an emission wavelength of 656 ± 5 and 745 ± 5 nm, respectively. The flat terrace region shows a strong PL emission of 656 nm, corresponding to the optical bandgap of 1.89 eV for bulk $BA_2MA_3Pb_4I_{13}$ (n = 4). However, we found the terrace edge exhibits an emission of 745 nm, which is corresponding to a smaller optical bandgap of 1.66 eV. We extracted the whole PL spectra from flat top-layer, bottom-layer and terrace edge regions, and compared them in **Figure 5F**. The flat terrace regions (flat top-layer and bottom-layer) display only one pronounce peak at 656 nm while the terrace edge region shows two peaks with a second peak at 745 nm. Hence, it is concluded that the terrace edge has a different electronic feature than their flat terrace counterpart. We further carried out the repeat CGM scan (**SI 9**) and found the TES current remains constant after 24 times scan and the topography of the terrace edge remains the same. These results

suggest the TES current might not related to ionic conduction effect, as ionic conduction consists of the transit of ions (atoms of positive or negative charge) from one site to another via point defects (site vacancies) in the crystal lattice. While at the TES, we did not observe lattice vacancies from the HRTEM results (**Figs. S3 a&b**). Repeating scan results also show no morphological change, which otherwise would be a direct result of ionic motion (mass transport).[27] In parallel, prior studies also revealed that the ionic motion is significantly suppressed in 2D halide perovskites.[28,29]

To further understand the increasing electronic conductivity at the TES. The electronic reconstruction picture was corroborated by first-principles density functional theory (DFT) calculations. Here we chose the simplest sample of BA_2PbI_4 (n = 1) as the model for simulation for consideration of calculation cost. The projected density of states (DOS) of bulk-BA_2PbI_4 has been firstly calculated, which is shown in **Fig. S16a**. The calculated bandgap of semiconductor BA_2PbI_4 is equal to 2.29 eV which is consistent well with the previous experimental results (2.43 eV).[30] For bulk BA_2PbI_4, the valence band (VB) is mainly contributed by orbital of I atoms, and the conduction band (CB) is mainly contributed by orbital of Pb atoms. Apart from this, we also constructed a surface structure (surface-BA_2PbI_4) along [001] direction with the 20 Å of vacuum layer (**Figure 6A**). Briefly, the terraces were introduced at the two PbI_4-terminated flat surfaces and the terrace width (W) was set as 6 unit cells to describe the TES effects. The projected DOS of surface-BA_2PbI_4 along the Pb-I planes are shown in **Fig. S16b**. Compare to the DOS in bulk-BA_2PbI_4 (**Fig. S16a**), the CB of surface-BA_2PbI_4 is shift down to the low-energy period, suggesting a lower forbidden bandwidth. This result is consistent with the red-shifted photoluminescence at TES in the confocal photoluminescence map (**Figures 5D, E**). Since the orbital of Pb atoms is the major contribution to CB, thus, we specifically calculate the projected DOS of Pb atoms at TES. As shown in **Figure 6B (i)**, we can find that near the Fermi level, the DOS of Pb1 atom (at the terrace edges) is much higher than those of other Pb atoms at flat terrace regions. To further quantify the DOS evolution across the terrace edge, we calculate the integral near Fermi level (0-0.3 eV) of the DOS of Pb atoms across terrace edge (**Figure 6B (ii)**). The order of the DOS integrals is Pb1>Pb2>Pb3>Pb4>Pb5>Pb6 and Pb1 at the edge exhibits significantly higher free electron density than other Pb atoms, indicating that the electronic conductivity is mainly contributed by the Pb atoms at terrace edge. Overall, the DFT calculation provides the fundamental

origins of the highly conductive TES in the low-dimensional perovskite, which is correlated with the atomic structural asymmetry and the electron orbital of the Pb atom at the edge.

3. Conclusion

In summary, we utilized the CGM measurement to visualize the highly conductive terrace edges in 2D, quasi-2D and 3D halide perovskite single-crystalline flakes. This direct contact electrical characterization revealed that the distinct conductive TES among the insulating terrace flat regions. The relative movement of the nanoscopic conductive tip at the crystal terrace edges generates the TES current without necessity of external bias. The TES current is intrinsically related with the crystal edge height and can be influenced by scanning speed and loading force applied on the tip. The current directions are reversible depending on the relative movement of the tip on the sample. Multiple characterization techniques including HRTEM, KPFM, CFM and CGM and first-principles density function theory (DFT) calculations demonstrate that the terrace edge CGM current at the crystal edge is not likely relevant to the ferroelectric domain wall or ionic contribution, it is more related to its intrinsic electronic properties that displaying lower Fermi-level and smaller bandgap. These findings are of great significance towards fundamental understanding of the crystal edge effect on charge transport in perovskite-based cells. Current generation only by mechanically sliding the nanoscopic conductive tip on the perovskite single-crystalline flakes provides new insights for triboelectric nanogenerator. Encoding the data information by templating the topographic patterns, followed by current readout will inspire the probe-based data storage technology.

4. Experimental Section

4.1 Single crystal growth

The free-standing single-crystalline flakes of 2D, quasi-2D and 3D halide perovskite were synthesized from the floating method according to our previous reports.[2] Briefly, 1.126 g, 2.4 mmol lead (II) oxide (Sigma-Aldrich, purity > 99.0%) was firstly dissolved in the mixed solution of 5 mL hydroiodic acid (Sigma-Aldrich, ≥57 wt.% in H_2O) and 800 μL hypophosphorous acid (Sigma-Aldrich, 50 wt. % in H_2O) at elevated temperature ~100 °C to form a pale-yellow solution. In another vial, stoichiometric methylammonium iodide (MAI, Luminescence Technology Corp) and *n*-butylamine (BA, Sigma-Aldrich, 99.5%) were slowly dissolved in 3 mL hydroiodic acid (HI)

in an ice-water bath. For example, for $BA_2MA_3Pb_4I_{13}$ (n=4), the mixed ammonium precursor-solution contains 1.2 mmol *n*-butylamine and 1.8 mmol MAI in 3 mL HI. After the formation of a transparent solution, the mixed ammonium precursor solution was slowly added into the lead solution under stirring. It should be noted that a higher temperature was provided by the hot-plate to sufficiently dissolve the solute for achieving an oversaturated solution. Then by slowly cooling down the hot solution at a slow rate of 0.5-5°C per hour, the crystallization first occurs at the water-air interface, followed by a horizontal growth. Depending on the precursor concentrations, time periods from minutes to hours were required to achieve centimeter sized single-crystalline flakes. The whole synthesis process was carried out in ambient conditions. The as-grown single crystal flakes were taken out from the solution, followed by drying overnight in a vacuum oven at 50 °C.

4.2 Characterization techniques

XRD patterns of single-crystalline flakes were obtained from a Philips Xpert Pro X-ray diffractometer (Almelo, The Netherlands) utilizing Cu Kα radiation. The SEM images were obtained from a Quanta 600 FEG. HRTEM imaging was conducted using a double aberration-corrected FEI Titan3 G2 60-300 at the Materials Characterization Laboratory (MCL) of the Materials Research Institute (MRI) in The Pennsylvania State University. We used FEI Titan at 80 kv with image corrector and Monochromator, the screen current of the electron beam was ~1 nA. Confocal Raman/fluorescence microscopic mapping measurement was performed on a WITec alpha500 equipped with a photodetector for photon collection. A laser with a wavelength of 633 nm was used as the incident beam connected by an optical fiber. For confocal Raman microscopic mapping purpose, we chose a BA_2PbI_4 (n = 1) sample as it has a larger bandgap than the incident photon energy thus the incident laser only induces vibrational and rotational Raman shift signals. For confocal fluorescence microscopic mapping purpose, we chose the $BA_2MA_3Pb_4I_{13}$ (n = 4) sample as it has a smaller bandgap than the incident photon energy, which will give a photoluminescence response of the sample. The KPFM was performed on Bruker Icon I with a PeakForce Kelvin Probe Force Microscopy mode. Before sample measurement, a freshly exfoliated HOPG (Highly Oriented Pyrolytic Graphite) reference was used for the calibration of the work function of the KPFM tip. The PFM measurement was also performed on Bruker Icon I, with a Piezo Response Microscopy mode. The I-V loop and dielectric constant *vs.* electric field measurement of a $BA_2MA_3Pb_4I_{13}$ (n = 4) single-crystal sample were performed on an electrochemical workstation (CH Instruments). Before the test, the crystal was firstly coated with

gold electrode using a vacuum thermal evaporation system (Covap from Angstrom Engineering), with the electrode area of 0.1 cm^2 controlled by a shadow mask.

4.3 CGM measurement

The CGM measurement was carried out on a pre-calibrated C-AFM setup (Park XE7 system) in contact mode. A platinum-coated silicon probes with tip radius of *ca.* 20 nm was used as the CGM tip. Both the tip and the samples were kept grounded for collecting the CGM signal. Various scan frequencies and load force were intentionally manipulated to obtain large signal noise ratios for each measurement. The single-crystalline perovskite flakes were orientated with the QW layer parallel to the substrate, hence the *z*-direction of the tip is perpendicular to the QW planes. The crystal orientation was verified by the XRD patterns. It should be noted that before the measurement, we exfoliate the sample surface to ensure a fresh top-surface being scanned by the CGM. The data collection was performed in dark ambient with a relative humidity of ~30% at room temperature.

4.4 FEM simulation

The electric field distribution at the tip/sample interface was simulated by the COMSOL Multiphysics software with a 2D electrostatic module. The CGM tip has a conical shape with a spherical apex of 20 nm radius. The contact geometry was determined by the Hertz model (detailed in **SI 5**). The relative dielectric constant was determined by **Equation S5** (**SI 5**) and used in the simulation. An initial potential of V = 850 mV was assigned to the contact interface according to the energy level difference between the tip and sample surface. Boundary condition at the sample end has the potential set to zero as was being grounded in the experiment.

4.5 DFT calculation

The ground-state electronic calculations were performed by Perdew-Burke-Ernzerhof (PBE) generalized gradient approximation (GGA) exchange-correlation implemented in the Vienna *ab* Initio Simulation Package (VASP).[27,28] The calculations use the PAW method and valence configurations include the H ($1s^1$), C($2s^22p^2$), N($2s^22p^3$), O ($2s^22p^4$), I ($5s^25p^5$) and Pb ($6s^26p^2$) states.[29] Electronic structure was described within a plane-wave basis with a kinetic energy cutoff of 400 eV. To explicitly account for van der Waals' interactions between BA^+ and Pb-I layers, Van der Waals-corrected D2 method of Grimme was used for all calculations.[34] For bulk structure, the lattice constants and atomic positions were both fully relaxed until a maximum energy difference and residual force on atoms converge were reached at 10^{-5} eV and 0.05 eV/Å,

respectively and the Brillouin zone was sampled with 8×8×4. Based on the calculated bulk BA_2PbI_4, the surface structure for calculation was constructed from a 6×1×1 lattice and a 20 Å vacuum layer stacked along the [001] direction. The residual force on atoms was changed to below 0.1 eV/Å for the surface calculation to make the structure easier to converge and the Brillouin zone was sampled with 1×2×1.

Associated content

Supporting Information is available online.

Author Contributions

K.W., T.W. and C.W. equally contribute to this work. K.W. and C.W. designed the experiments. T.W. performed the calculation. K.W. and C.W. synthesized the materials and performed the XRD, HRTEM, SEM, KPFM, etc., measurements. Y.J. performed the CGM experiments. R.S. performed the FEM simulations. All the authors were actively involved in the discussion and analysis of the data. K.W. and T.W. wrote the manuscript. S.P. supervised the project.

Acknowledgments

S.P. acknowledge financial support from Office of Naval Research through grant number N000141712520. R.S. acknowledges the financial support from National Science Foundation through grant number ECCS-1832865. K.W. and D.Y. acknowledge the financial support from Air Force Office of Scientific Research under award number <FA9550-17-1-0341>. Y.Y. acknowledges support from National Science Foundation through award number IIP-1832179.

References

1 J. Byun, H. Cho, C. Wolf, M. Jang, A. Sadhanala, R. H. Friend, H. Yang and T.-W. Lee, *Adv. Mater.*, 2016, **28**, 7515–7520.

2 K. Wang, C. Wu, D. Yang, Y. Jiang and S. Priya, *ACS Nano*, 2018, **12**, 4919–4929.

3 G. Grancini, C. Roldán-Carmona, I. Zimmermann, E. Mosconi, X. Lee, D. Martineau, S. Narbey, F. Oswald, F. De Angelis, M. Graetzel and M. K. Nazeeruddin, *Nat. Commun.*, 2017, **8**, 15684.

4 P. Li, Y. Chen, T. Yang, Z. Wang, H. Lin, Y. Xu, L. Li, H. Mu, B. N. Shivananju, Y. Zhang, Q. Zhang, A. Pan, S. Li, D. Tang, B. Jia, H. Zhang and Q. Bao, *ACS Appl. Mater. Interfaces*, 2017, **9**, 12759–12765.

5 W.-J. Yin, J.-H. Yang, J. Kang, Y. Yan and S.-H. Wei, *J. Mater. Chem. A*, 2015, **3**, 8926–8942.

6 K. Wang, D. Yang, C. Wu, M. Sanghadasa and S. Priya, *Prog. Mater. Sci.*, 2019, 100580.

7 E. Shi, Y. Gao, B. P. Finkenauer, A. Akriti, A. H. Coffey and L. Dou, *Chem. Soc. Rev.*, 2018, 47, 6046–6072.

8 G. Grancini, V. D'Innocenzo, E. R. Dohner, N. Martino, A. R. Srimath Kandada, E. Mosconi, F. De Angelis, H. I. Karunadasa, E. T. Hoke and A. Petrozza, *Chem. Sci.*, 2015, **6**, 7305–7310.

9 S. Ahmad, C. Hanmandlu, P. K. Kanaujia and G. V. Prakash, *Opt. Mater. Express*, 2014, **4**, 1313.

10 D. Hong, S. Wan and Y. Tian, *J. Lumin.*, 2017, **192**, 1191–1195.

11 L. Peng, Y. Yuan, G. Li, X. Yang, J.-J. Xian, C.-J. Yi, Y.-G. Shi and Y.-S. Fu, *Nat. Commun.*, 2017, **8**, 659.

12 K. C. Nowack, E. M. Spanton, M. Baenninger, M. König, J. R. Kirtley, B. Kalisky, C. Ames, P. Leubner, C. Brüne, H. Buhmann, L. W. Molenkamp, D. Goldhaber-Gordon and K. A. Moler, *Nat. Mater.*, 2013, **12**, 787–791.

13 C. Tao, L. Jiao, O. V. Yazyev, Y.-C. Chen, J. Feng, X. Zhang, R. B. Capaz, J. M. Tour, A. Zettl, S. G. Louie, H. Dai and M. F. Crommie, *Nat. Phys.*, 2011, **7**, 616–620.

14 J.-C. Blancon, H. Tsai, W. Nie, C. C. Stoumpos, L. Pedesseau, C. Katan, M. Kepenekian, C. M. M. Soe, K. Appavoo, M. Y. Sfeir, S. Tretiak, P. M. Ajayan, M. G. Kanatzidis, J. Even, J. J. Crochet and A. D. Mohite, *Science*, 2017, **355**, 1288–1292.

15 Y. Wang, C. Wang, X. Su, V. G. Hadjiev, H. A. C. Benavides, Y. Ni, M. K. Alam, F. C. Robles-Hernandez, Y. Yao, S. Chen, Z. Wang and J. Bao, 2018, arxiv.org/abs/1803.11490.

16 E. Shi, S. Deng, B. Yuan, Y. Gao, Akriti, L. Yuan, C. S. Davis, D. Zemlyanov, Y. Yu, L. Huang and L. Dou, *ACS Nano*, 2019, **13**, 1635–1644.

17 S. Hong, S. Tong, W. I. Park, Y. Hiranaga, Y. Cho and A. Roelofs, *Proc. Natl. Acad. Sci. U. S. A.*, 2014, **111**, 6566–9.

18 S. Tong, I. W. Jung, Y.-Y. Choi, S. Hong and A. Roelofs, *ACS Nano*, 2016, **10**, 2568–2574.

19 K. Wang, C. Wu, Y. Jiang, D. Yang, K. Wang and S. Priya, *Sci. Adv.*, 2019, **5**, eaau3241.

20 K. Wang, D. Yang, C. Wu, J. Shapter and S. Priya, *Joule*, 2019, **3**, 311–316.

21 Y.-Y. Choi, S. Tong, S. Ducharme, A. Roelofs and S. Hong, *Sci. Rep.*, 2016, **6**, 25087.

22 W. J. Yin, T. Shi and Y. Yan, *Appl. Phys. Lett.*, 2014, **104**, 063903.

23 O. G. Reid, K. Munechika and D. S. Ginger, *Nano Lett.*, 2008, **8**, 1602–1609.

24 R. Kraya, L. Y. Kraya and D. A. Bonnell, *Nano Lett.*, 2010, **10**, 1224–1228.

25 J. Y. Park and M. Salmeron, *Chem. Rev.*, 2014, **114**, 677–711.

26 J. Liu, A. Goswami, K. Jiang, F. Khan, S. Kim, R. McGee, Z. Li, Z. Hu, J. Lee and T. Thundat, *Nat. Nanotechnol.*, 2018, **13**, 112–116.

27 Y. Shao, Y. Fang, T. Li, Q. Wang, Q. Dong, Y. Deng, Y. Yuan, H. Wei, M. Wang, A. Gruverman, J. Shield and J. Huang, *Energy Environ. Sci.*, 2016, **9**, 1752–1759.

28 Y. Lin, Y. Bai, Y. Fang, Q. Wang, Y. Deng and J. Huang, *ACS Energy Lett.*, 2017, **2**, 1571–1572.

29 X. Xiao, J. Dai, Y. Fang, J. Zhao, X. Zheng, S. Tang, P. N. Rudd, X. C. Zeng and J. Huang, *ACS Energy Lett.*, 2018, **3**, 684–688.

30 M. I. Saidaminov, O. F. Mohammed and O. M. Bakr, *ACS Energy Lett.*, 2017, **2**, 889–896.

31 G. Kresse and J. Hafner, *Phys. Rev. B*, 1994, **49**, 14251–14269.

32 G. Kresse and J. Furthmüller, *Phys. Rev. B*, 1996, **54**, 11169–11186.

33 P. E. Blöchl, *Phys. Rev. B*, 1994, **50**, 17953–17979.

34 S. Grimme, *J. Comput. Chem.*, 2006, **27**, 1787–1799.

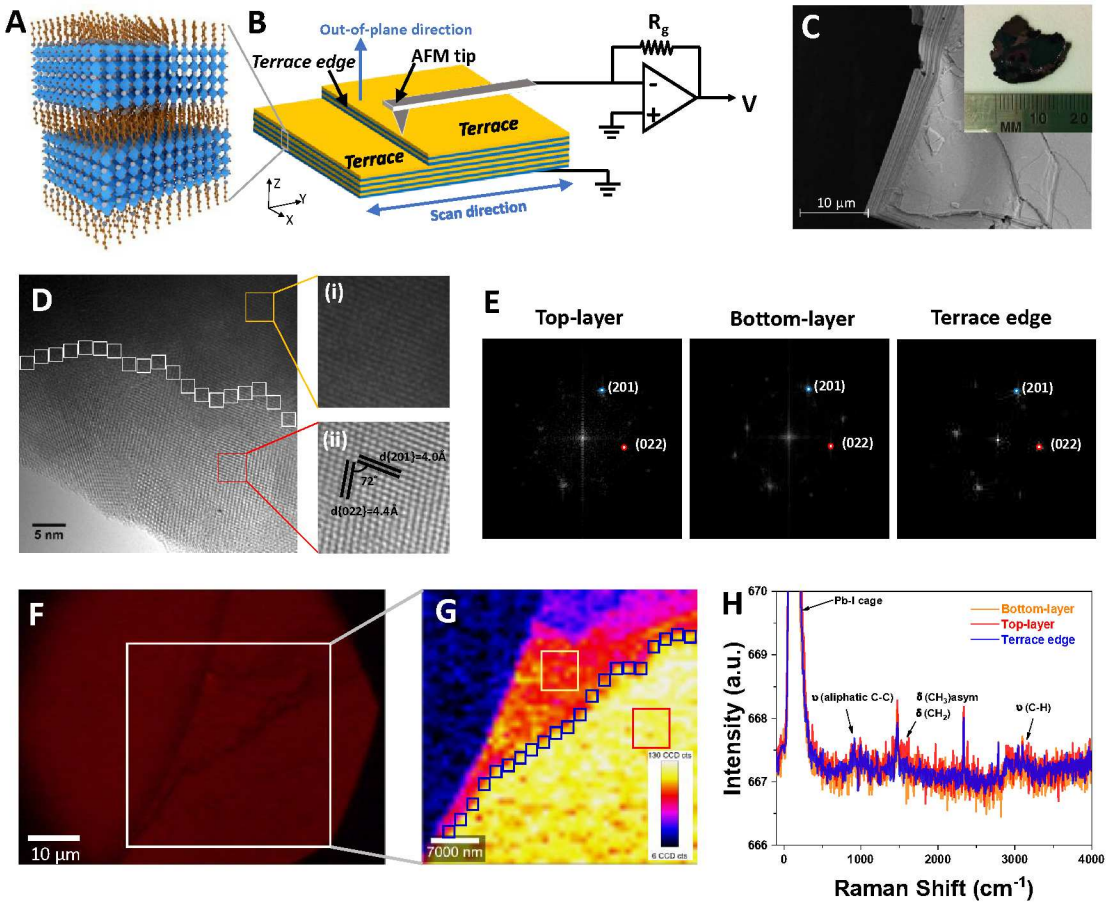

Figure 1. Experimental layout for the CGM measurement and identification of layer edge. (A) Schematic showing an MQW structure of a quasi-2D halide perovskite of $BA_2MA_3Pb_4I_{13}$ ($n = 4$). **(B)** Diagram of CGM measurement testing a single-crystal flake of quasi-2D halide perovskite. The quasi-2D flake was orientated with the out-of-plane direction in parallel with the *z*-direction (vertical direction) of the CGM. **(C)** The corresponding SEM image showing a laminar feature, inset: a photo showing a centimeter sized quasi-2D halide perovskite of $BA_2MA_3Pb_4I_{13}$ ($n = 4$). **(D)** HRTEM image of $BA_2MA_3Pb_4I_{13}$ ($n = 4$) perovskite with yellow square denoting the *i)* top-layer region, red the *ii)* bottom-layer region and white the terrace edge regions. **(E)** The FFT patterns of different geometric regions. Confocal Raman measurement on single crystals samples. **(F)** Optical-microscopy images with a square showing the Raman mapping region. **(G)** Confocal Raman map probed at a Raman shift of 94 cm^{-1}. **(H)** Comparison of Raman spectra obtained from different regions.

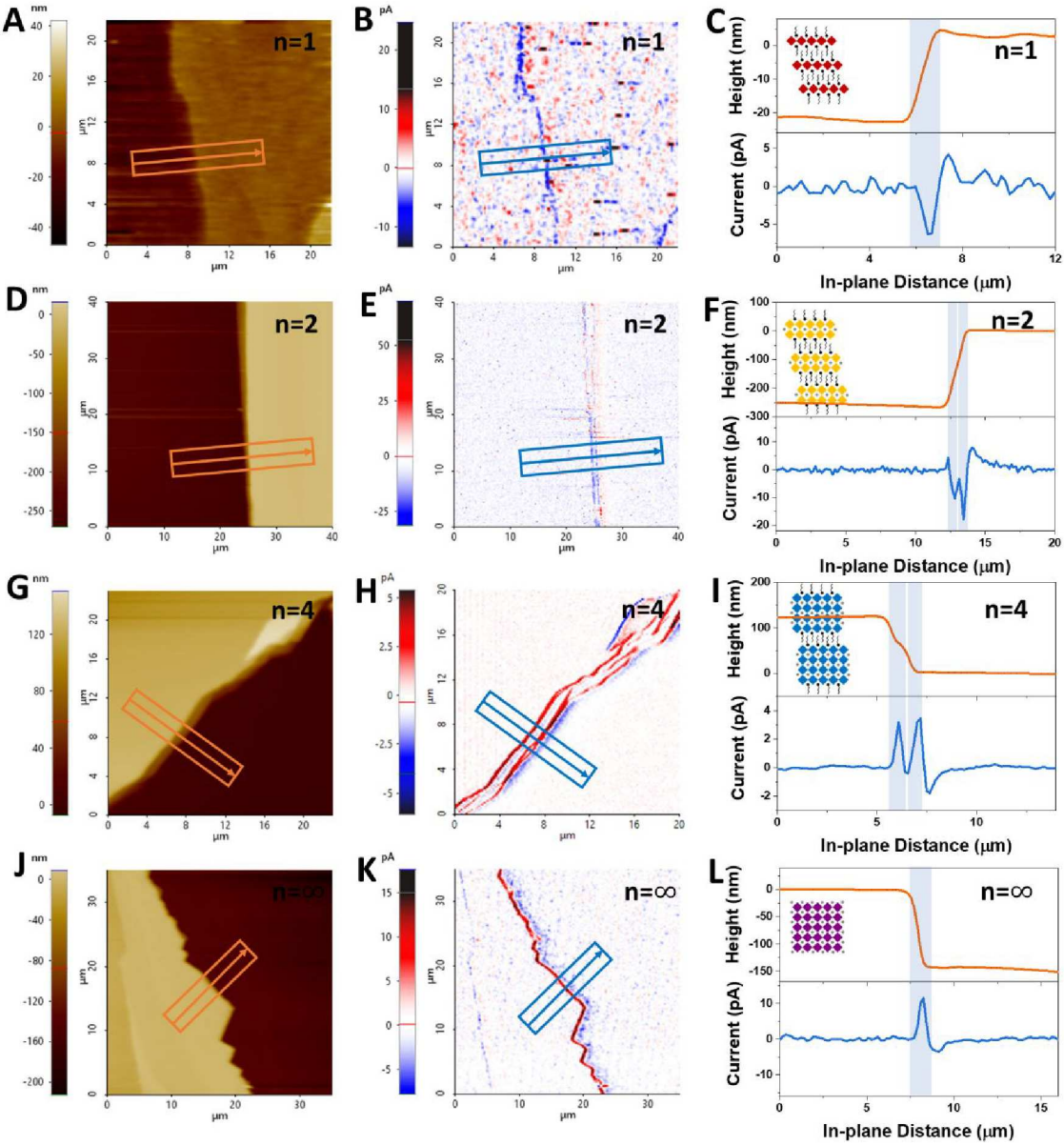

Figure 2. CGM results of 2D (n = 1), quasi-2D (n = 2, 4) and 3D (n = ∞) halide perovskite. (A, D, G, J) Topographical image of different samples, **(B, E, H, K)** the corresponding current images, **(C, F, I, L)** the corresponding average line profile measured along the arrow direction from the topographical and current images of each sample.

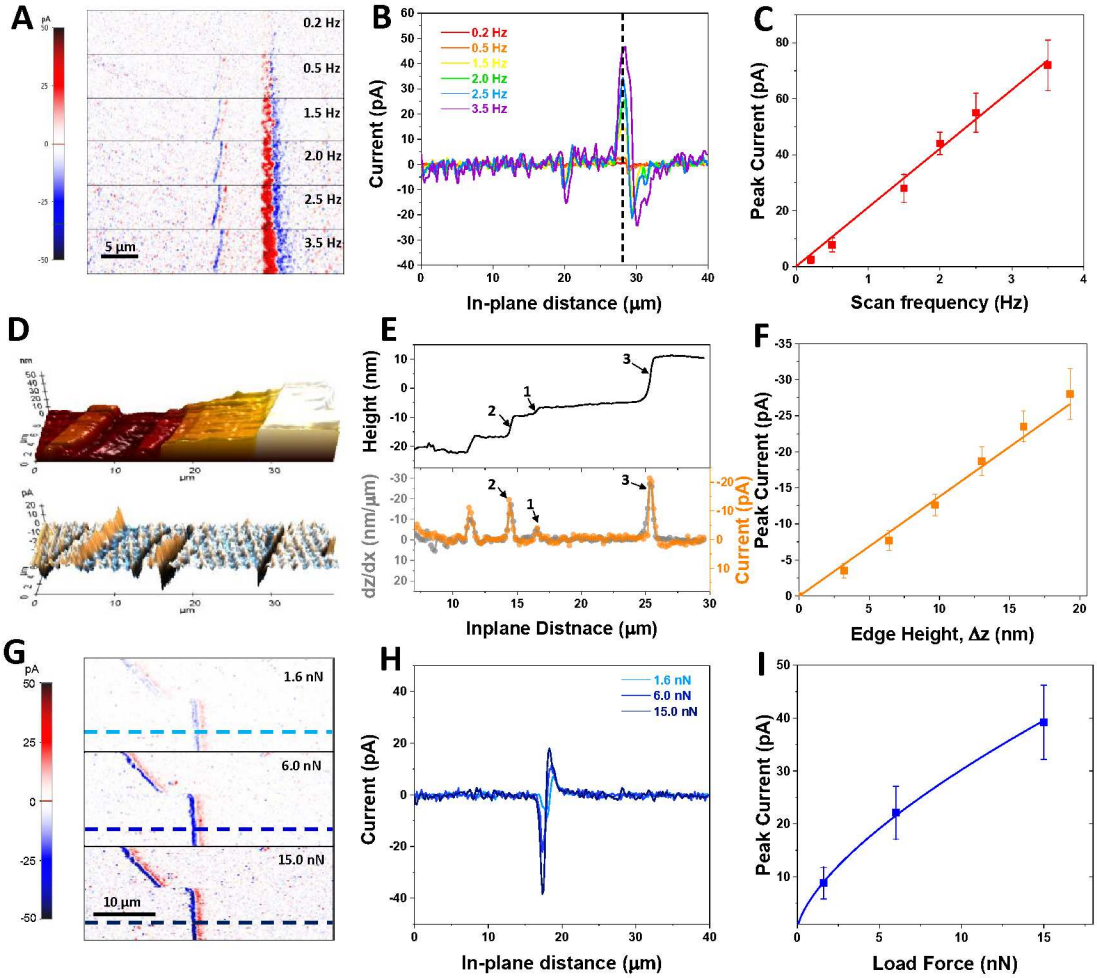

Figure 3. Study of the effect of scan frequency, edge height and load force on the detected TES current. Scan frequency effect: **(A)** CGM current images under different scan frequencies, **(B)** the average current profile along the in-plane *x*-direction, **(C)** peak current (current values at x = 28.3 μm, dash line in (B)) dependence on the scan frequency. Edge height effect: **(D)** 3D CGM topography and current images showing different edge height (top panel) and hence different edge current (bottom panel), **(E)** average height profile, first derivative of height profile (dz/dx) and current profile along the in-plane *x*-direction, **(F)** peak current dependence on the edge height (Δz). Load force effect: **(G)** CGM current images under different load forces, **(H)** average current profile along the dash line in (G), **(I)** peak current dependence on the load force.

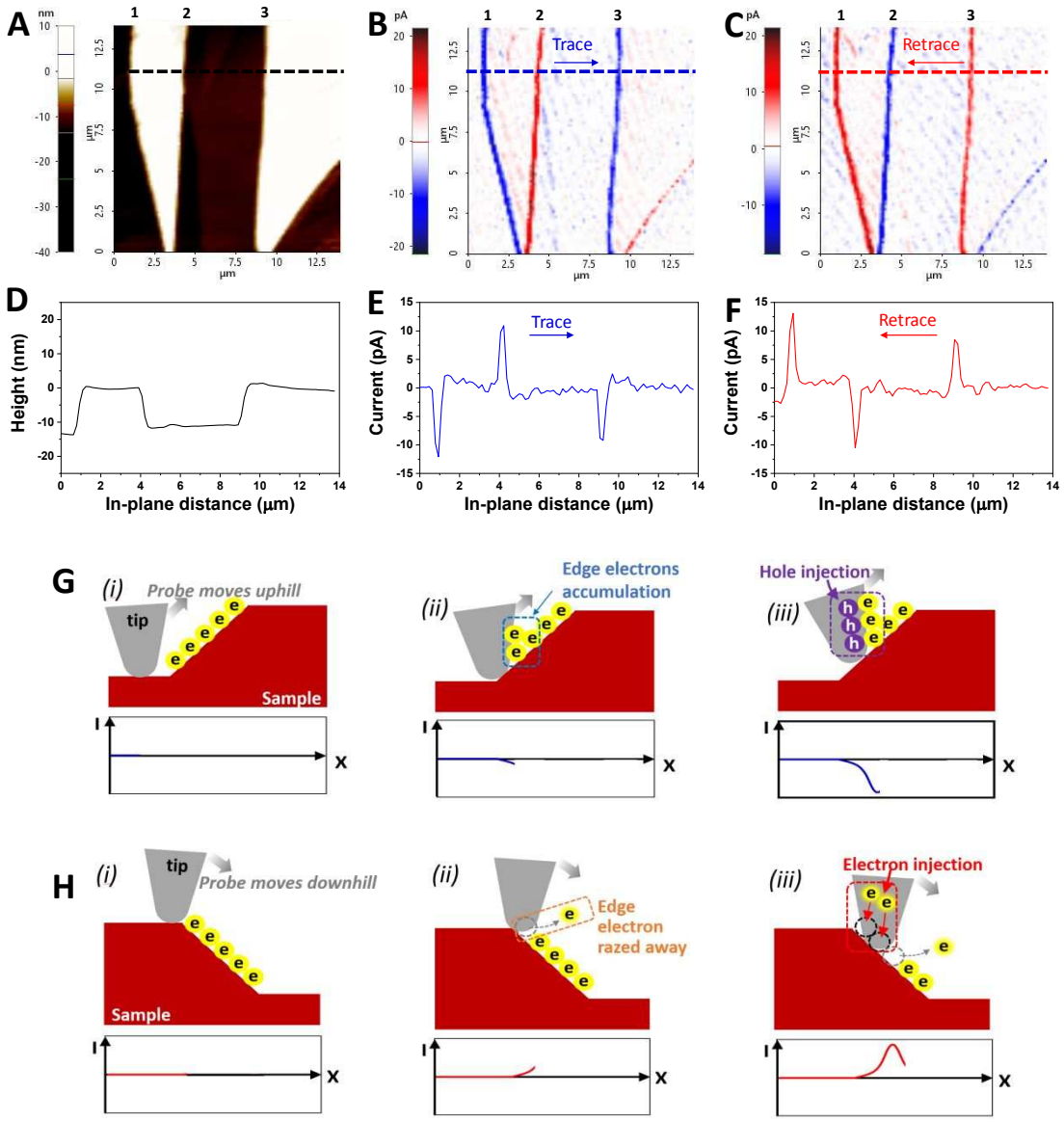

Figure 4. Study of current direction by trace and retrace scan on different topographies. (A) CGM topography image showing lineaments with raised and depressed regions. CGM current image with **(B)** trace (from left to right) and **(C)** retrace (from right to left) scan directions. Corresponding line profile of **(D)** height, **(E)** trace current and **(F)** retrace current obtained from corresponding CGM images. Schematic diagram of CGM contrast mechanism based on the electron refilling and consumption during the probe moving **(G)** uphill and **(H)** downhill the terrace edges at different positions *i)* terrace, *ii)* starting of edge, and *iii)* middle of edge.

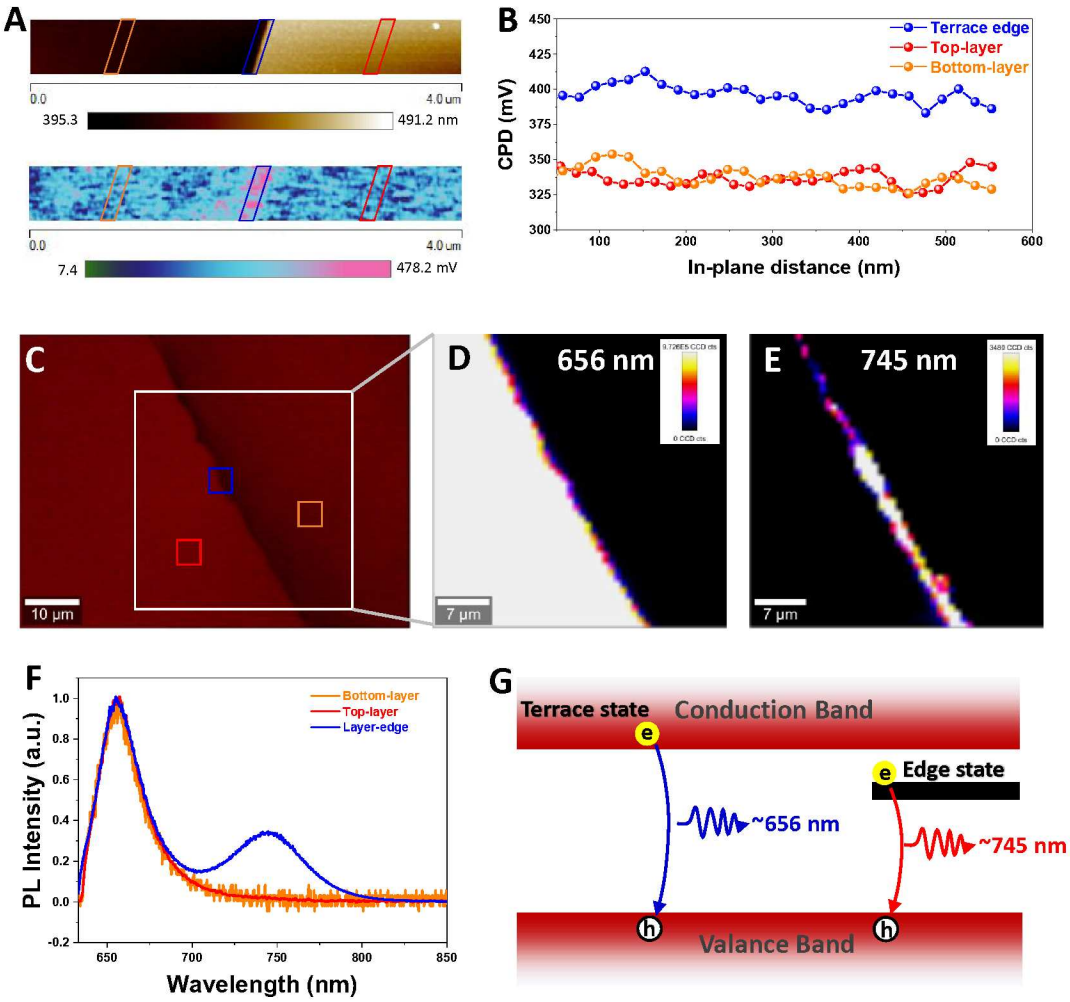

Figure 5. Surface potential and photoluminescence at terrace edge regions of quasi-2D perovskite. (A) Topography and contact potential difference (CPD) images, recorded by Kelvin probe force microscopy (KPFM). **(B)** Average CPD profile at different regions (corresponding to the denoted parallelograms in (a)). Confocal fluorescence microscopy (CFM) measurement. **(C)** Optical-microscopy images showing the Raman mapping region. CFM mapping probed at emission wavelength of **(D)** 656 nm and **(E)** 745 nm. **(F)** Photoluminescence (PL) spectra extracted from top-layer, bottom-layer and terrace edge regions (denoted by red, yellow and blue squares in (D)). **(G)** Energy band schematic showing the energy level of the flat terrace state and terrace edge state.

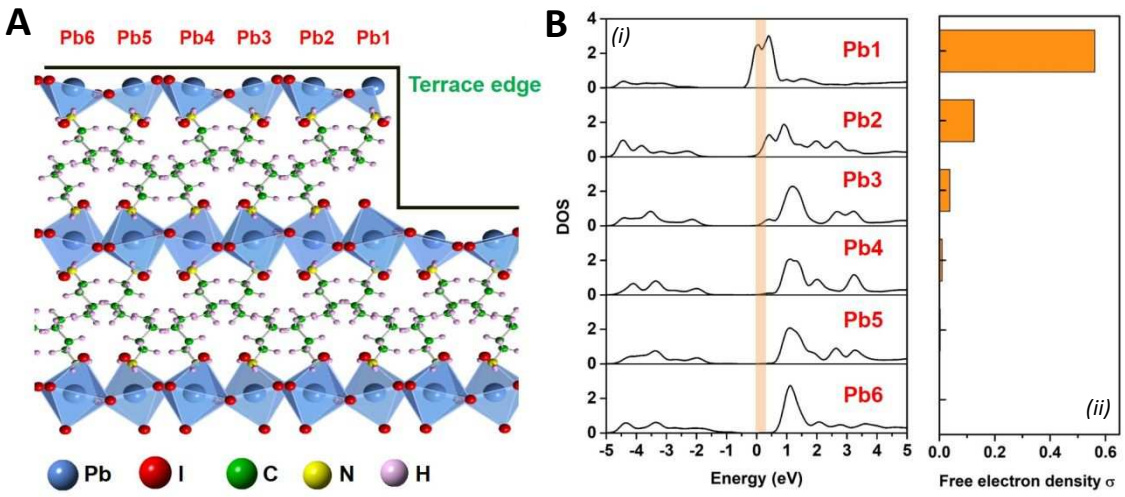

Figure 6. First-principle DFT calculation. (A) Schematic lattice of a surface-BA_2PbI_4 supercell constructed for first-principles calculations. **(B)** *(i)* The density of states (DOS) profiles and free-electron densities of the Pb-I planes in surface-BA_2PbI_4. *(ii)* The right panel is the free electron density calculated from the DOS near fermi level (0-0.3 eV).

Distinct terrace edge current has been firstly detected in quasi-2D perovskite by charge gradient microscopic (CGM) measurement, which is due to the structural asymmetry at the edge in these materials.

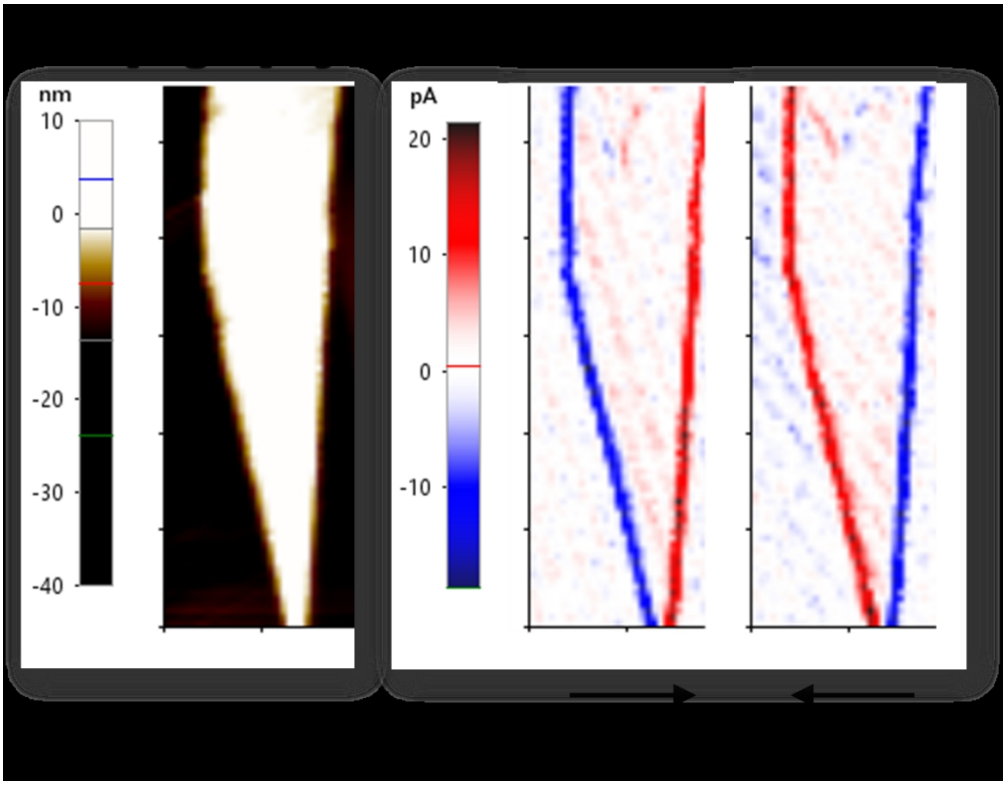
nm
10
0
-10
-20
-30
-40
pA
20
10
0
-10